


ORIGINAL RESEARCH

Open Access



Feasibility of imaging synaptic density in the human spinal cord using [^{11}C]UCB-J PET

Samantha Rossano^{1,2*} , Takuya Toyonaga¹, Jason Bini¹, Nabeel Nabulsi¹, Jim Ropchan¹, Zhengxin Cai¹, Yiyun Huang¹ and Richard E. Carson^{1,2}

*Correspondence:

samantha.rossano@yale.edu

¹ Department of Radiology and Biomedical Imaging, Yale PET Center, Yale School of Medicine, P.O. Box 208048, New Haven, CT 06520, USA
Full list of author information is available at the end of the article

Abstract

Purpose: Neuronal damage and synapse loss in the spinal cord (SC) have been implicated in spinal cord injury (SCI) and neurodegenerative disorders such as Amyotrophic Lateral Sclerosis (ALS). Current standards of diagnosis for SCI include CT or MRI imaging to evaluate injury severity. The current study explores the use of PET imaging with [^{11}C]UCB-J, which targets the synaptic vesicle protein 2A (SV2A), in the human spinal cord, as a way to visualize synaptic density and integrity in vivo.

Results: First, simulations of baseline and blocking [^{11}C]UCB-J HRRT scans were performed, based on SC dimensions and SV2A distribution to predict V_T , V_{ND} , and V_S values. Next, human baseline and blocking [^{11}C]UCB-J HRRT images were used to estimate these values in the cervical SC (cSC). Simulation results had excellent agreement with observed values of V_T , V_{ND} , and V_S from the real human data, with baseline V_T , V_{ND} , and V_S of 3.07, 2.15, and 0.92 mL/cm³, respectively, with a BP_{ND} of 0.43. Lastly, we explored full SC imaging with whole-body images. Using automated SC regions of interest (ROIs) for the full SC, cSC, and thoracic SC (tSC), the distribution volume ratio (DVR) was estimated using the brain gray matter as a reference region to evaluate SC SV2A density relative to the brain. In full body imaging, DVR values of full SC, cSC, and tSC were 0.115, 0.145, and 0.112, respectively. Therefore, measured [^{11}C]UCB-J uptake, and thus SV2A density, is much lower in the SC than in the brain.

Conclusions: The results presented here provide evidence for the feasibility of SV2A PET imaging in the human SC, however, specific binding of [^{11}C]UCB-J is low. Ongoing and future work include further classification of SV2A distribution in the SC as well as exploring higher-affinity PET radioligands for SC imaging.

Keywords: Synaptic density, SV2A, Spinal cord, PET

Background

The central nervous system (CNS) is comprised of the brain and the spinal cord and is responsible for transmitting nerve signals that control critical functions in the body, such as locomotion and respiration. The spinal cord (SC) has a key role in relaying nerve signals between the periphery and the brain, and also can respond to external stimuli by spinal reflex. The integrity of SC neurons and synapses is crucial for proper function, and traumatic spinal cord injury (SCI) or neurodegenerative diseases may lead to

interruption or loss of these functions. Specifically, physical damage to the SC in traumatic SCI disrupts neural circuits and in turn results in loss of functions that depend on the location of the lesion. Studies have shown that functional recovery may be possible, depending on the severity of the injury [1, 2]. Synapse loss in the spinal cord has also been suggested in the pathology of amyotrophic lateral sclerosis (ALS), a neurodegenerative disease that causes dysfunction and eventually total loss of function in neural circuits crucial for movement, speech, and breathing [3]. Additionally, synapse loss in the spinal cord has been shown in mouse models of spinal muscular atrophy, an autosomal recessive disease that causes atrophy and muscle weakness resulting from motor neuron death [4]. Synaptic pathologies of these conditions are typically studied in animal models, as there have been no methods to study synaptic density *in vivo*.

Clinical imaging techniques, such as computed tomography (CT) and magnetic resonance imaging (MRI), have been studied for evaluation of spinal cord conditions [5–7]. These methods aid in visualizing and assessing the degree of structural lesions, and functional MRI techniques can explore the physiological function and protein composition of the tissue surrounding the site of injury. Positron emission tomography (PET) is a functional imaging modality which quantifies physiological properties of tissue *in vivo*. Synaptic vesicle glycoprotein 2A (SV2A) is the target of interest for novel PET radiotracers, and imaging with this ligand can assess synaptic density in the living brain [8], as SV2A exists in presynaptic vesicles ubiquitously across the brain [9]. [¹¹C]UCB-J, a SV2A PET radioligand, has been used to explore SV2A differences in clinical populations including epilepsy [10], depression [11], and Alzheimer's disease [12, 13]. Thus, measures from SV2A PET are sensitive to synaptic loss and pathologies in various brain diseases and disorders.

Although SV2A as a marker for synaptic density in the brain has been studied robustly, SV2A as a marker for synaptic density in the spinal cord has not been well established. Previous studies report SV2A expression in the rodent spinal cord, at concentrations 2-to-fivefold lower than the cortex [14]. Since SV2A is expressed in the mammalian spinal cord, it is possible that the full CNS may be of potential interest for SV2A PET imaging studies. However, this is not without challenges. Given the limitations of whole body PET imaging, such as poor spatial resolution that contributes to partial volume effects (PVE), small structures and lower concentration of protein in the spinal cord, and the dependence on high affinity radioligands for quantitative accuracy, PET imaging in the spinal cord remains an area for which more optimization is needed before it can be utilized as a clinical tool. If useful, SV2A PET imaging in the spinal cord can provide ways to evaluate synaptic integrity of patients with SCI, ALS, or other neurodegenerative disorders, and can aid in diagnosis and prognosis of these conditions, along with potential utility in assessing treatment efficacy, based on functional synapse density.

The current study explores the use of [¹¹C]UCB-J PET for *in vivo* evaluation of synaptic density in the spinal cord by imaging SV2A in human spinal cord. Firstly, a simulation study was completed to model the capability of imaging SV2A in the spinal cord at the resolution of the high-resolution brain PET scanner, the High-Resolution Research Tomograph (HRRT). Next, human baseline and blocking [¹¹C]UCB-J images acquired on the HRRT were used to evaluate SV2A blocking and V_{ND} in the cervical spinal cord. Lastly, total body images aided in the visualization of [¹¹C]UCB-J distribution in the

full spinal cord, and was quantified using the simplified reference tissue model (SRTM) to generate distribution volume ratios (DVR) of spinal cord radioactivity in relation to brain gray matter binding.

Methods

Simulation of SV2A in the spinal cord

A simulation study was designed to evaluate the ability of using [¹¹C]UCB-J PET to measure SV2A blocking and V_{ND} in the spinal cord (SC) at a resolution comparable to the Siemens High Resolution Research Tomograph (HRRT). Prior studies have shown that SV2A concentrations are 3–to-fivefold lower in the spinal cord (SC) than in the cortex [14]. Knowing that the PET outcome measure of total volume of distribution is the total of the nondisplaceable PET binding and the specific PET binding ($V_T = V_{ND} + V_S$), we can simulate the V_T in the gray matter (GM), white matter (WM) and full SC using the following assumptions: 1) as $V_S^{SC} = 0.2 * V_S^{Cortex}$, 2) volumetrically, the SC is ~75% WM and ~25% GM [15], 3) V_S is minimal in the WM (~0.00 mL/cm³), and 4) V_{ND} is the same across brain and SC GM at approximately 2.8 mL/cm³ [16]. Prior studies suggest that V_{ND} in the white matter is slightly greater than in the GM, at about 3.3 mL/cm³, however, for this simulation, V_{ND} was assumed to be uniform across gray and white matter. The assumptions and definitions of the parameters in this simulation are outlined in Table 1. V_T images of the SC under baseline and blocking with 75% receptor occupancy (r) conditions were generated with the full spinal cord as an ellipse with radii of 3 voxels (~3.6 mm) and 5 voxels (~6.1 mm). Voxels were assigned as white or gray matter to mimic the cord, with gray matter centered. Simulated baseline and blocking images were blurred using a Gaussian filter (4 mm FWHM), which is the estimated resolution at the edge of the axial field of view of the HRRT, based on estimations from line source phantom studies (data not shown). The simulated V_T values under baseline and blocking conditions were calculated for the full SC ROI and for voxels outside the spinal cord (non-cord), and observed V_{ND} and V_S values for the full SC were calculated as described in Eqs. 1 and 2, derived from the occupancy plot equation [17], where r is assumed known:

Table 1 Table of definitions and assumptions for simulation study

Parameter definition	Cortex	Spinal cord (SC) gray matter (GM)	Spinal cord (SC) white matter (WM)	Full spinal cord (SC) ~ 3:1 WM:GM [15]
Relative SV2A concentration, based on ex vivo SV2A concentrations [14]	1.00	0.20	0.00	
V_{ND} , Nondisplaceable Volume of Distribution	2.80	2.80	2.80	2.80
V_S , Specific Volume of Distribution of SV2A	17.2	3.44	0.00	0.81
Baseline V_T , Total Volume of Distribution = $V_{ND} + V_S$	20.0 ^a	6.24	2.80	3.83
Blocking V_T (75% occupancy), Total Volume of Distribution = $V_{ND} + (1 - r) * V_S$	7.10	3.66	2.80	3.06

^a Approximate mean GM V_T [19]

$$V_{ND}^{Observed} = \frac{(V_T^{Baseline} - V_T^{Blocking}) - r * V_T^{Baseline}}{r} \quad (1)$$

$$V_S^{Observed} = V_T^{Baseline} - V_{ND}^{Observed} \quad (2)$$

Cervical spinal cord imaging on the HRRT

Four human research participants (2 M/2F, 24–46 years) completed PET scanning with [¹¹C]UCB-J on the Siemens HRRT under baseline conditions and blocking conditions with either Levetiracetam (LEV) or Brivaracetam (BRV). These scans were selected from a cohort of subjects previously published [16, 18], based on the positioning of the head in the scanner, such that both baseline and blocking images included at least ~20 mm (>20 axial slices) of cervical spinal cord at the end of the FOV. Arterial blood sampling, PET data collection and image reconstruction were completed as described previously [16, 18]. On an early summed PET image (0–10 min), the location of the cervical spinal cord (cSC) was manually defined, and a cylindrical ROI with radius = 3 voxels (~4 mm) was generated along 15 axial slices (~18.5 mm). The cSC ROI for a representative subject is shown in Additional file 1. Time activity curves (TACs) of this region were fit with a 1-tissue compartment model (1TCM) to estimate V_T in the cSC in baseline and blocking scans. Parametric images of V_T were generated by voxel-wise fitting of the 1TCM as described previously [19]. For each subject, regional brain V_T estimates from both baseline and blocking scans were used to estimate SV2A occupancy using the Lassen Occupancy Plot [17]. The observed occupancy from the Lassen plot was used along with the baseline and blocking cSC V_T in Eqs. 1 and 2 to calculate observed V_{ND} and V_S in the cSC.

Full spinal cord imaging on the mCT

PET scans used for this portion of the study were acquired and published for dosimetry purposes previously [20]. Four human research participants (2 M, 2F, 26–47 years) completed PET/CT scanning on the Siemens mCT with [¹¹C]UCB-J as described previously [20]. Arterial blood sampling was not performed. CT images were acquired prior to PET scanning and were used for attenuation correction and scatter correction [21], as well as ROI definition. Dynamic PET scanning with [¹¹C]UCB-J was completed using continuous bed motion with the following frame times: 4 × 60 s, 2 × 120 s, 23 × 5 min. PET images were reconstructed using time of flight (TOF) and point spread function (PSF) modeling and ordered subset expectation maximization (OSEM) algorithm with 2 iterations, 21 subsets (Siemens Medical Solutions, USA). A summed standardized uptake value (SUV) image (30–60 min) was used to threshold brain uptake to define a gray matter (GM) ROI (MR images were not available).

The spinal cord ROI was defined using the CT image. Firstly, the CT image was cropped to include the SC, starting from the base of the skull to the L2/L3 vertebrae. The voxels with intensities similar to bone were binarized into a mask. This spine mask was closed to fill holes within and between vertebrae by dilating and eroding the binary mask with a kernel with radius of 5 voxels. The Center of Mass in x (COMx) and y (COMy) directions were calculated on each axial slice, and a cubic spline was used to fit COMx

and COMy. Then, on each axial slice, a circular ROI with radius of 2 voxels (~ 4 mm) was generated around this point and a full SC ROI mask was generated. This process is described in Additional file 2. A cervical SC (cSC) was defined from the full SC ROI from the C2 to C6 vertebrae. A thoracic SC (tSC) was defined from the full SC ROI from T2 to T10 vertebrae.

The full SC ROI TAC was fit with the simplified reference tissue model (SRTM2 [22]), using the whole brain GM as a reference region and a fixed k_2' value of 0.018 min^{-1} [19], based on previously published values. Kinetic analysis was completed using 60 min of dynamic PET data for all regional TACs. The distribution volume ratio (DVR) was estimated to explore $[^{11}\text{C}]\text{UCB-J}$ uptake in the SC relative to the brain GM, and should equal $V_T^{\text{SC}}/V_T^{\text{GM}}$.

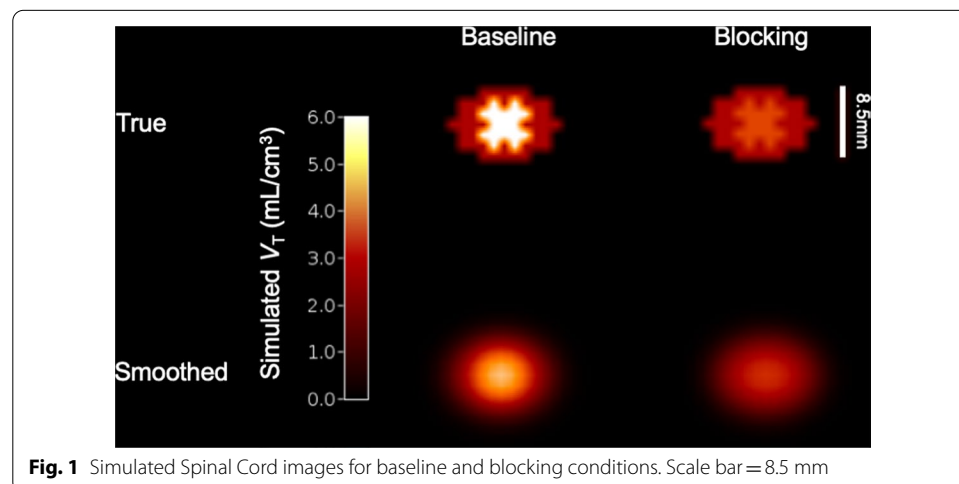
Results

Simulation of SV2A in the spinal cord

Simulated True and Smoothed baseline and blocking images are shown in Fig. 1. The true values of baseline and blocking V_T values were 3.83 and 3.06 mL/cm^3 , respectively, for the full SC (Table 1), and 0.0 and 0.0 mL/cm^3 for the non-cord. After smoothing, the measured baseline and blocking V_T values were 3.09 and 2.36 mL/cm^3 , respectively, for the full SC and 0.02 mL/cm^3 and 0.02 mL/cm^3 for the non-cord. With the simulated occupancy of 75%, using Eqs. 1 and 2, the $V_{\text{ND}}^{\text{observed}}$ based on these measured ROI estimates is 2.12 mL/cm^3 and the V_S^{observed} is 0.97 mL/cm^3 .

Cervical spinal cord imaging on the HRRT

Whole brain and cSC V_T images from baseline and blocking scans from a representative subject are shown in Fig. 2 in a color scale optimized for whole brain V_T (top row) and the cSC V_T (bottom row). Across the four subjects, the mean (s.d., range) brain GM occupancy was 78.4% (8.6%, 65–85%), the mean GM V_{ND} was 2.65 mL/cm^3 (0.39, 2.28–3.08), the mean baseline cSC V_T was 3.07 mL/cm^3 (0.87, 2.23–4.29) and the mean blocking cSC V_T was 2.36 mL/cm^3 (0.11, 2.22–2.45). The mean $V_{\text{ND}}^{\text{observed}}$ was 2.15 mL/cm^3 (0.24, 1.99–2.50) and the mean V_S^{observed} was 0.92 mL/cm^3 (1.06, -0.26 –2.30). Thus.



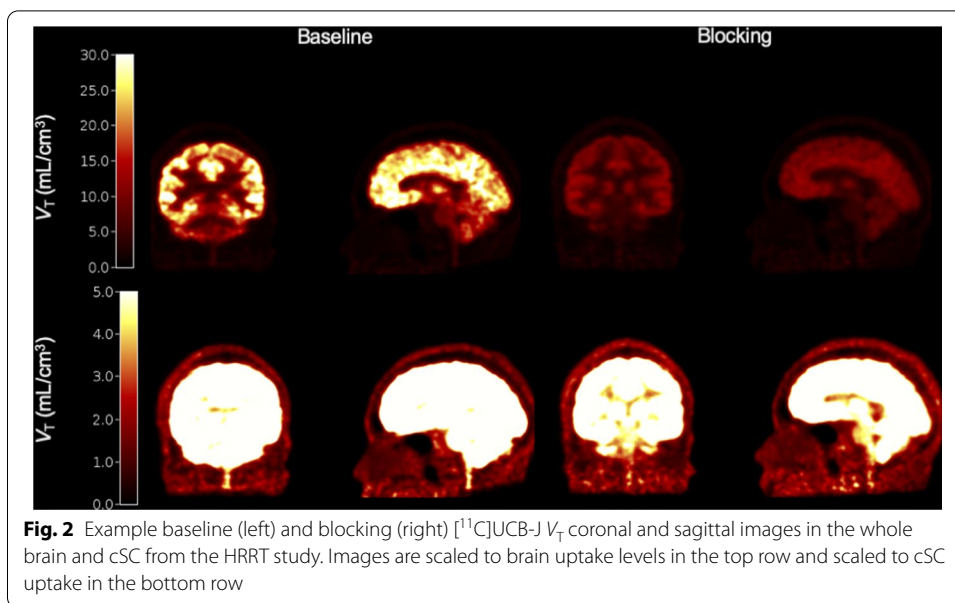


Table 2 Comparison of outcome measures between simulation study and occupancy study

	Occupancy Study (Mean, $N=4$)	Simulation study	% Difference, $(\text{Occ} - \text{Sim})/\text{Sim} * 100$
Baseline V_T (mL/cm ³)	3.07	3.09	-0.6
Blocking V_T (mL/cm ³)	2.36	2.36	-0.2
V_{ND} (mL/cm ³)	2.15	2.12	1.3
V_S (mL/cm ³)	0.92	0.97	-4.7
BP_{ND}	0.43	0.46	-6.5

the cSC binding potential ($BP_{\text{ND}} = V_S/V_{\text{ND}}$) is 0.43. These results strongly agree with the results from the Simulation study above (Table 2). The mean cSC V_T estimates were 9.1% and 14.6% lower than simulated values at baseline and blocking, respectively. The mean V_{ND} observed in the human data was about 16% lower than the simulated results, whereas the mean V_S was about 13% greater than the simulated results.

Full spinal cord imaging in the mCT

An example automated SC ROI is shown in Fig. 3. $[^{11}\text{C}]\text{UCB-J}$ uptake in the SC was $78 \pm 5\%$ less than in the whole brain gray matter (peak SUV = 1.9 g/mL in the SC vs. 8.7 g/mL). The SRTM2 fit of the full SC ROI TAC from an example subject is shown in Fig. 4. Using SRTM2, the mean (\pm SD) DVR (Full SC/brain GM) in the SC was 0.115 (\pm 0.020). The mean DVR in the cSC was 0.145 (\pm 0.051) and the mean DVR in the tSC was 0.112 (\pm 0.016). The individual and mean parameter estimates from SRTM2 for all ROIs are shown in Table 3. DVR represents the ratio of the total volume of distribution between the region of interest and the reference region; in this case, $\text{SC DVR} = V_T^{\text{SC}}/V_T^{\text{Cortex}}$. Multiplying the mean DVR in the cSC reported here by the approximate V_T in the cortex of ~ 20.0 mL/cm³, an estimated V_T^{SC} value is 2.90 mL/cm³, which is about 5% less than the mean cSC baseline V_T reported in the human data

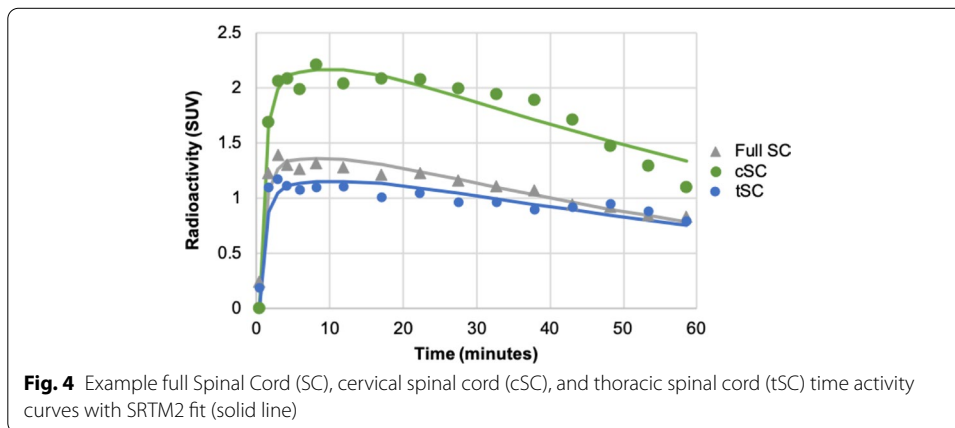
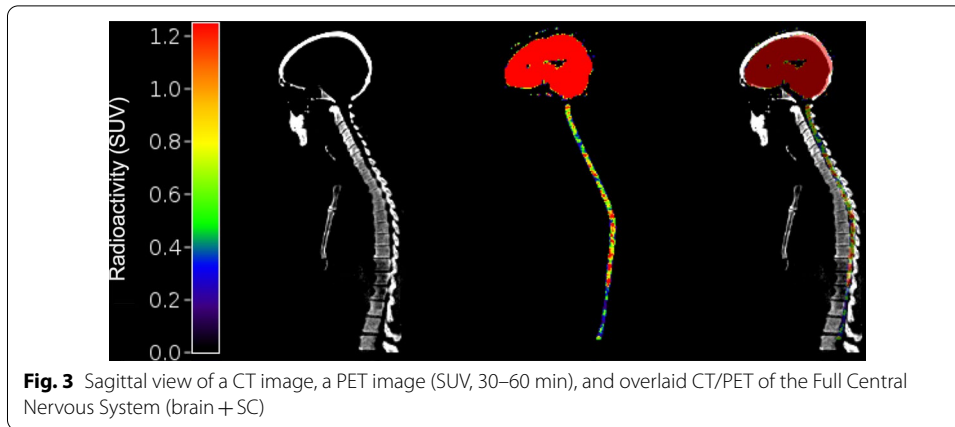


Table 3 Parameter estimates (%standard error) from SRTM2 fits of automated SC, cSC, and tSC ROI TACs for individual subjects along with mean and SD for 4 subjects

	<i>DVR</i>	<i>R</i> ₁	<i>k</i> ₂
<i>Full SC</i>			
Subject 1	0.115 (10.7)	0.231 (8.80)	0.036 (15.7)
Subject 2	0.094 (6.83)	0.268 (6.70)	0.051 (10.6)
Subject 3	0.142 (3.73)	0.204 (2.45)	0.026 (5.31)
Subject 4	0.107 (5.45)	0.150 (3.71)	0.025 (7.77)
Mean (S.D.)	0.115 (0.020)	0.213 (0.049)	0.035 (0.012)
<i>Cervical SC (cSC)</i>			
Subject 1	0.143 (7.35)	0.205 (5.20)	0.026 (10.7)
Subject 2	0.074 (7.47)	0.221 (7.30)	0.054 (11.6)
Subject 3	0.181 (10.7)	0.201 (5.89)	0.020 (14.8)
Subject 4	0.183 (4.26)	0.237 (2.77)	0.023 (6.04)
Mean (S.D.)	0.145 (0.051)	0.216 (0.016)	0.031 (0.016)
<i>Thoracic SC (tSC)</i>			
Subject 1	0.103 (12.3)	0.213 (10.2)	0.037 (18.1)
Subject 2	0.104 (7.13)	0.293 (7.00)	0.051 (11.1)
Subject 3	0.135 (5.49)	0.210 (3.78)	0.028 (7.87)
Subject 4	0.104 (7.60)	0.124 (4.68)	0.021 (10.7)
Mean (S.D.)	0.112 (0.016)	0.210 (0.069)	0.034 (0.013)

above, suggesting good agreement in imaging and quantification methods across the two scanners.

Discussion

This study explores the feasibility of imaging SV2A in the spinal cord with [^{11}C]UCB-J PET. Firstly, baseline and blocking PET data were simulated using previously defined SV2A concentrations in the SC relative to the cortex of $\sim 20\%$ [14], conditions of 75% blocking, and the partial volume effect. Given a true V_{ND} of 2.8 mL/cm^3 [16], and assuming no specific binding in the WM, calculated baseline and blocking V_{T} values were 3.09 and 2.36 mL/cm^3 , respectively, with an observed V_{ND} of 2.12 mL/cm^3 . The simulation suggested that specific binding of [^{11}C]UCB-J in the spinal cord is low, with an expected BP_{ND} of 0.46 . Next, we evaluated specific [^{11}C]UCB-J binding in the cSC under baseline and blocking conditions from scans acquired in four human subjects on the HRRT. The observed V_{T} , V_{ND} , and V_{S} values agreed exceptionally well with the simulated measures, with an expected BP_{ND} value of 0.43 . Lastly, we explored the feasibility of full SC imaging using whole body [^{11}C]UCB-J PET/CT images acquired on the mCT. CT images were used to automatically define ROIs for the full, cervical, and thoracic SC. DVR estimates in these regions show that [^{11}C]UCB-J uptake in the full SC relative to cortical GM is 0.115 . Interestingly, a higher DVR was observed in the cSC than in the tSC, with DVRs of 0.145 and 0.112 , respectively. The DVR in the cSC agreed well with the ratio of baseline V_{T} in the SC relative to the brain, with a ratio of approximately 0.154 from the HRRT study. Although the pattern of heterogeneity within the SC has not been well established in the synaptic density literature, it is the same pattern that has been reported in [^{18}F]FDG images of the human spinal cord as imaged with PET/CT and PET/MRI [23–26]. The consistency across imaging methods in this study suggests that SV2A may be imaged in the human SC, but [^{11}C]UCB-J may not be an ideal PET tracer to use for this purpose, due to its low specific binding.

The current study implemented PET data acquired across two different scanners—the Siemens HRRT for brain/cSC imaging and the Siemens Biograph mCT for full SC imaging—each with different spatial resolutions. For each set of images, the whole SC ROIs were defined in different ways. On the HRRT images, the cSC ROI was defined on an early PET image. On the mCT images, the SC was defined based on the CT image. For both cases, the ROI included the whole SC, consisting of GM in the center of the cord surrounded by WM. A vast majority of the specific SV2A signal is located at the center of the ROI in the GM, with low-to-negligible concentrations of SV2A in the WM. Because of this, the effect of the resolution difference across the two scanners will likely be small, and the PVE caused by the respective spatial resolutions should not drastically affect our quantitation of the SC. Any activity that may spill over from the high activity GM voxels will spill into the relatively low activity WM voxels, which are also included in the SC ROI. The results presented in this work support this premise, particularly in regards to the similarities of SV2A PET measures in the cSC across images of different resolution.

However, PVE may be of importance given different SV2A concentrations and potential differences in radiotracer properties between GM and WM in the SC. The cross section of the SC, including both WM and GM, is elliptical with diameters of about 9 mm

in the anteroposterior direction and 12 mm in the transverse direction in the cervical segment and diameters of 6 mm and 9 mm, respectively, in the thoracic segments [27]. Since the human spinal cord is approximately 75% WM by volume [15], if the cross-sectional area of the full cSC is $\sim 84.8 \text{ mm}^2$, then approximately $\sim 21.2 \text{ mm}^2$ or 25% of the full cSC volume will be comprised of GM. Given a PET system with resolution at about 4–5 mm, isolating GM signal from the full cord is impossible without the use of partial volume correction. Of the many advantages to PET/MR imaging in the spinal cord [28], MR images can aid in partial volume correction to isolate PET signals from the spinal cord, the CSF and other surrounding tissues. With fine enough resolution on the MRI, distinction of the GM and WM in the spinal cord may be possible, but this was not feasible with the MRIs acquired for brain images in the current study. In addition, the contrast of GM to WM signal of ^{11}C UCB-J is much lower than what is observed in the brain, due to a lower SV2A concentration in SC, as has been reported in rodents [14]. This lower GM/WM contrast will reduce the potential degree of PVE observed within the SC.

In analyzing the *in vivo* occupancy study of SV2A in the cSC, the V_T estimates at baseline and blocking conditions were estimated using 1-tissue compartment model fitting of cSC TACs. ROIs of the cSC were located at the axial edge of the HRRT FOV (since the brain was centered), which has lower sensitivity for gamma ray detection due to smaller solid angle available at this positioning inside the PET scanner. In addition to higher noise, out of field scatter can affect the image quality and quantitation at this location, potentially leading to inaccuracies in the estimates presented here. In the whole-body images, the tSC is particularly sensitive to scatter correction accuracy due to the proximity to the liver, which has very high ^{11}C UCB-J uptake. Inaccurate scatter correction in this region of the image would lead to misestimation of radioactivity concentration in the tSC. In addition to scatter, subject motion may also have an effect on the quantitation of PET radioactivity, particularly in the case of respiratory motion in whole body PET images. Furthermore, using PSF modeling with OSEM image reconstruction methods may increase potential edge or Gibbs artifacts that cause quantitative inaccuracies in PET images, in a manner that is dependent on number of iterations, pixel size, and object size [29]. The effects of these limitations should be explored further, to confirm the current study reports of $\sim 20\%$ lower ^{11}C UCB-J DVR in the tSC. In any case, blocking studies in whole body scanning (with arterial blood sampling) may aid in evaluation of specific SV2A binding and V_{ND} throughout the full SC.

Although it is part of the central nervous system, the spinal cord differs from the brain particularly in their interaction with circulation. In the brain, the blood–brain barrier (BBB) is a layer of endothelial cells that surround blood vessels in the brain, which have unique characteristics such as lacking fenestrations in cell membranes and tight junctions between cells. The BBB regulates transport of molecules from circulation into brain tissue, particularly keeping larger and more polar particles from entering the brain tissues. Similar to those in brain, blood vessels in the spinal cord have a blood-spinal cord barrier (BSCB), though it is believed that the BSCB may be more permeable than the BBB [30]. This may be of particular interest given that previous studies have suggested that radiometabolites of ^{11}C UCB-J do not pass the BBB [19], but uptake of radiometabolites in the SC tissue is not yet well studied,

and may be possible depending on the size or polarity of radiometabolites as well as the permeability of the BSCB. The current study uses 60 min of dynamic PET data to evaluate [^{11}C]UCB-J uptake in both cSC images from the HRRT and full SC images on the mCT, which limits the potential effects on the PET measures of radiometabolites, which tend to increase in relative concentration throughout the scan.

Furthermore, there is another difference between the brain and SC that is important to note, especially when using reference tissue methods to quantify PET images of the SC as implemented here. The current study defined a SC ROI that included both GM and WM, while the reference region utilized with SRTM2 was comprised of whole brain GM only. Previous work using [^{11}C]UCB-J has reported lower K_1 estimates in WM than in GM regions of the brain [19]. Given that the SC is a majority WM by volume, the K_1 relative to the brain GM, or the R_1 estimate, may be low due to this difference. This is likely the reason why the R_1 estimates that resulted from SRTM2 analysis of the whole-body full SC were low, on the scale of about 0.2 (Table 3). This should be considered when using reference region quantification methods in the future study of SC PET imaging.

Although the results presented in this study are somewhat encouraging, there is additional work that can be done to validate or improve our findings. For example, ex vivo experiments may be completed to confirm SV2A density throughout the cervical, thoracic or full SC. Our group has completed preliminary Western blotting experiments to investigate the concentration of SV2A in the cSC compared to SV2A in gray matter regions of one 13 y.o. male rhesus monkey. The resulting SC/brain SV2A ratio, equivalent to a V_S ratio (assuming no difference in K_d), was about 0.057. Given that SV2A density may be up to fivefold lower in the GM of the SC compared to that of the cortex, and that only 25% of the SC is comprised of GM, this ratio strongly agrees with an estimated relative SV2A concentration in the SC of $0.2(0.25) = 0.05$. Using the V_S estimates from our brain imaging data reported in Tables 1 and 2, we report a SC/brain V_S ratio of approximately 0.056. Further studies are needed to explore if, and to what extent, SV2A changes throughout the length of the spinal cord.

SV2A image quality in the SC may be enhanced by improving PET scanner resolution. Given the dimensions of the SC, a PET system with ~ 3 mm resolution or better is crucial for successful imaging of the SC. SV2A PET radiotracers labeled with fluorine-18, such as [^{18}F]SynVesT-1 [31], will result in higher quality PET images due to lower statistical noise. Furthermore, new radiotracers with less metabolism, or radiotracers with affinity greater than that of [^{11}C]UCB-J ($K_d < \sim 3$ nM) may also improve the quantification of SV2A PET in the spinal cord. As described above, the B_{\max} in the full SC is expected to be ~ 20 -fold lower than the cerebral cortex. To get a more useful measure of BP_{ND} (i.e., ~ 5 times greater than the BP_{ND} estimates of ~ 0.45 in the current study), the K_d of an SV2A radioligand should be at least 5 times lower than that of [^{11}C]UCB-J (assuming no change in nondisplaceable uptake). Furthermore, additional radioligands that target other proteins or physiological functions of interest aside from SV2A, such as the serotonin transporter with [^{11}C]AFM [32] or the 18 kDa translocator protein (TSPO) with [^{11}C]PK11195 [33] or [^{18}F]GE-180 [34], may be worthwhile in characterizing spinal cord pathophysiology.

Conclusions

The current study suggests that PET imaging with [^{11}C]UCB-J is a feasible way to measure synaptic density by SV2A in the human spinal cord. Results from simulation and human studies showed a consistent, albeit low, SV2A binding potential in the cord. Although future work is needed to validate specific binding and distribution of SV2A in the full SC, the results presented here show that imaging SV2A in the SC is possible. If validated, this imaging technique can be used to noninvasively evaluate the synaptic integrity of the SC in clinical populations including spinal cord injury, or spinal cord diseases like ALS, and may also be helpful in monitoring treatment progression.

Abbreviations

ALS: Amyotrophic lateral sclerosis; BBB: Blood brain barrier; BP_{ND} : Binding potential in relation to the nondisplaceable compartment; BSCB: Blood spinal cord barrier; cSC: Cervical spinal cord; CT: Computed tomography; DVR: Distribution volume ratio; FOV: Field of view; GM: Gray matter; HRRT: High-resolution research tomograph; PET: Positron emission tomography; PVE: Partial volume effect; SC: Spinal cord; SCl: Spinal cord injury; SRTM2: Simplified reference tissue model 2; SV2A: Synaptic vesicle glycoprotein 2A; TAC: Time activity curve; tSC: Thoracic spinal cord; V_{ND} : Nondisplaceable volume of distribution; V_{S} : Specific volume of distribution; V_{T} : Total volume of distribution; WM: White matter.

Supplementary Information

The online version contains supplementary material available at <https://doi.org/10.1186/s40658-022-00464-0>.

Additional file 1. Region of interest definition on HRRT PET Images - Top row: Sagittal view of early (0-10 mins) summed baseline (left) and blocking (right) [^{11}C]UCB-J PET uptake images scaled to brain uptake (A) and scaled to spinal cord uptake (B). Bottom row: Cervical spinal cord ROI (cylinder of 3 voxel radius along 15 axial slices) is shown in green overlaid on the early PET image.

Additional file 2. Automated region of interest definition on mCI PET Images - (A) A single slice of a cropped anatomical CT image. (B) Binarized cropped CT image including voxels including vertebrae. (C) Closed, binarized cropped CT image including vertebrae and spinal cavity. (D) Difference image between (C) and (D) including spinal cavity. The Center of Mass in x- and y- directions was calculated on each axial slice of this image, and COMx and COMy were fit with a cubic spline. (E) A single slice of a continuous, full SC ROI mask.

Acknowledgements

The authors acknowledge the faculty and staff of the Yale PET Center for their assistance in this study. We also acknowledge Dr. Ming-Kai Chen for discussions that supported the preparation of this manuscript.

Author contributions

SR performed data analysis and prepared manuscript. TT performed experiments, data analysis. JB designed the study assisted with data analysis. ZC designed the study, assisted with data analysis. NN, JR, YH designed the study. REC designed the study, data analysis, and prepared manuscript. All authors read and approved the final manuscript.

Funding

Financial support was received from R01NS094253 and S10RR029245. This publication was made possible by CTSA grant UL1 RR024139 from the National Center for Advancing Translational Sciences (NCATS), a component of the National Institutes of Health (NIH). Its contents are solely the responsibility of the authors and do not necessarily represent the official view of NIH.

Availability of data and materials

Code, data and material used and/or analyzed in this study can be made available by the corresponding author with reasonable request.

Declarations

Ethics approval and consent to participate

The portion of this study involving human data was approved by the Yale Human Investigation Committee, the Yale New Haven Hospital Radiation Safety Committee, and in accordance with the United States federal policy for the protection of human research contained in Title 45 Part 46 of the Code of Federal Regulations (45 CFR 46). All procedures performed were in accordance with the ethical standards of the institution and/or national research committee and with the 1964 Helsinki Declaration and its later amendments or comparable ethical standards. The studies for which human subjects were involved were approved by the Yale University Human Investigation Committee and Radiation Safety Committees. Informed consent was obtained from all individual participants included in the study.

Consent for publication

Not applicable.

Competing interests

The authors have no conflicts to disclose.

Author details

¹Department of Radiology and Biomedical Imaging, Yale PET Center, Yale School of Medicine, P.O. Box 208048, New Haven, CT 06520, USA. ²Department of Biomedical Engineering, Yale University, New Haven, CT, USA.

Received: 10 June 2021 Accepted: 20 April 2022

Published online: 03 May 2022

References

1. Darian-Smith C. Synaptic plasticity, neurogenesis, and functional recovery after spinal cord injury. *Neuroscientist*. 2009;15:149–65. <https://doi.org/10.1177/1073858408331372>.
2. Raineteau O, Schwab ME. Plasticity of motor systems after incomplete spinal cord injury. *Nat Rev Neurosci*. 2001;2:263–73. <https://doi.org/10.1038/35067570>.
3. Fogarty MJ. Amyotrophic lateral sclerosis as a synaptopathy. *Neural Regen Res*. 2019;14:189–92. <https://doi.org/10.4103/1673-5374.244782>.
4. Tarabal O, Caraballo-Mirallas V, Cardona-Rossinyol A, Correa FJ, Olmos G, Llado J, et al. Mechanisms involved in spinal cord central synapse loss in a mouse model of spinal muscular atrophy. *J Neuropathol Exp Neurol*. 2014;73:519–35. <https://doi.org/10.1097/NEN.000000000000074>.
5. Freund P, Seif M, Weiskopf N, Friston K, Fehlings MG, Thompson AJ, et al. MRI in traumatic spinal cord injury: from clinical assessment to neuroimaging biomarkers. *Lancet Neurol*. 2019;18:1123–35. [https://doi.org/10.1016/S1474-4422\(19\)30138-3](https://doi.org/10.1016/S1474-4422(19)30138-3).
6. Seif M, Gandini Wheeler-Kingshott CA, Cohen-Adad J, Flanders AE, Freund P. Guidelines for the conduct of clinical trials in spinal cord injury: Neuroimaging biomarkers. *Spinal Cord*. 2019;57:717–28. <https://doi.org/10.1038/s41393-019-0309-x>.
7. El Mendili MM, Querin G, Bede P, Pradat PF. Spinal cord imaging in amyotrophic lateral sclerosis: historical concepts–novel techniques. *Front Neurol*. 2019;10:350. <https://doi.org/10.3389/fneur.2019.00350>.
8. Finnema SJ, Nabulsi NB, Eid T, Detyniecki K, Lin SF, Chen MK, et al. Imaging synaptic density in the living human brain. *Sci Transl Med*. 2016;8:348ra96. <https://doi.org/10.1126/scitransmed.aaf6667>.
9. Bajjalieh SM, Frantz GD, Weimann JM, McConnell SK, Scheller RH. Differential expression of synaptic vesicle protein 2 (SV2) isoforms. *J Neurosci*. 1994;14:5223–35.
10. Finnema SJ, Toyonaga T, Detyniecki K, Chen MK, Dias M, Wang Q, et al. Reduced synaptic vesicle protein 2A binding in temporal lobe epilepsy: A [(11)C]UCB-J positron emission tomography study. *Epilepsia*. 2020;61:2183–93. <https://doi.org/10.1111/epi.16653>.
11. Holmes SE, Scheinost D, Finnema SJ, Naganawa M, Davis MT, DellaGioia N, et al. Lower synaptic density is associated with depression severity and network alterations. *Nat Commun*. 2019;10:1529. <https://doi.org/10.1038/s41467-019-09562-7>.
12. Chen MK, Mecca AP, Naganawa M, Finnema SJ, Toyonaga T, Lin SF, et al. Assessing synaptic density in Alzheimer disease with synaptic vesicle glycoprotein 2A positron emission tomographic imaging. *JAMA Neurol*. 2018;75:1215–24. <https://doi.org/10.1001/jamaneurol.2018.1836>.
13. Mecca AP, Chen MK, O'Dell RS, Naganawa M, Toyonaga T, Godek TA, et al. In vivo measurement of widespread synaptic loss in Alzheimer's disease with SV2A PET. *Alzheimers Dement*. 2020;16:974–82. <https://doi.org/10.1002/alz.12097>.
14. Lambeng N, Gillard M, Vertongen P, Fuks B, Chatelain P. Characterization of [(3)H]ucb 30889 binding to synaptic vesicle protein 2A in the rat spinal cord. *Eur J Pharmacol*. 2005;520:70–6. <https://doi.org/10.1016/j.ejphar.2005.07.029>.
15. Henmar S, Simonsen EB, Berg RW. What are the gray and white matter volumes of the human spinal cord? *J Neurophysiol*. 2020;124:1792–7. <https://doi.org/10.1152/jn.00413.2020>.
16. Rossano S, Toyonaga T, Finnema SJ, Naganawa M, Lu Y, Nabulsi N, et al. Assessment of a white matter reference region for (11)C-UCB-J PET quantification. *J Cereb Blood Flow Metab*. 2020;40:1890–901. <https://doi.org/10.1177/0271678X19879230>.
17. Cunningham VJ, Rabiner EA, Slifstein M, Laruelle M, Gunn RN. Measuring drug occupancy in the absence of a reference region: the Lassen plot re-visited. *J Cereb Blood Flow Metab*. 2010;30:46–50. <https://doi.org/10.1038/jcbfm.2009.190>.
18. Finnema SJ, Rossano S, Naganawa M, Henry S, Gao H, Pracitto R, et al. A single-center, open-label positron emission tomography study to evaluate rivaracetam and levetiracetam synaptic vesicle glycoprotein 2A binding in healthy volunteers. *Epilepsia*. 2019;60:958–67. <https://doi.org/10.1111/epi.14701>.
19. Finnema SJ, Nabulsi NB, Mercier J, Lin SF, Chen MK, Matuskey D, et al. Kinetic evaluation and test-retest reproducibility of [(11)C]UCB-J, a novel radioligand for positron emission tomography imaging of synaptic vesicle glycoprotein 2A in humans. *J Cereb Blood Flow Metab*. 2018;38:2041–52. <https://doi.org/10.1177/0271678X17724947>.
20. Bini J, Holden D, Fontaine K, Mulnix T, Lu Y, Matuskey D, et al. Human adult and adolescent biodistribution and dosimetry of the synaptic vesicle glycoprotein 2A radioligand (11)C-UCB-J. *EJNMMI Res*. 2020;10:83. <https://doi.org/10.1186/s13550-020-00670-w>.
21. Watson CC. Extension of single scatter simulation to scatter correction of time-of-flight PET. *IEEE Trans Nucl Sci*. 2007;54:1679–86. <https://doi.org/10.1109/TNS.2007.901227>.

22. Wu Y, Carson RE. Noise reduction in the simplified reference tissue model for neuroreceptor functional imaging. *J Cereb Blood Flow Metab.* 2002;22:1440–52. <https://doi.org/10.1097/01.WCB.0000033967.83623.34>.
23. Do BH, Mari C, Tseng JR, Quon A, Rosenberg J, Biswal S. Pattern of 18F-FDG uptake in the spinal cord in patients with non-central nervous system malignancy. *Spine (Phila Pa 1976).* 2011;36:E1395–401. <https://doi.org/10.1097/BRS.0b013e31820a7df8>.
24. Aiello M, Alfano V, Salvatore E, Cavaliere C, Picardi M, Della Pepa R, et al. [(18)F]FDG uptake of the normal spinal cord in PET/MR imaging: comparison with PET/CT imaging. *EJNMMI Res.* 2020;10:91. <https://doi.org/10.1186/s13550-020-00680-8>.
25. Guner LA, Unal K, Vardareli E, Kaya E, Temiz H, Dayioglu T. Physiological fluorodeoxyglucose uptake of spinal cord in adults. *Nucl Med Commun.* 2020;41:659–65. <https://doi.org/10.1097/MNM.0000000000001188>.
26. Patel NJ, Gupta V, Vibhute PG, Jain MK, Accurso JM. A large cohort study of 18f fluoro-deoxy-glucose uptake in normal spinal cord: quantitative assessment of the contamination from adjacent vertebral marrow uptake and validity of normalizing the cord uptake against the Lumbar Thecal Sac. *J Comput Assist Tomogr.* 2017;41:125–30. <https://doi.org/10.1097/RCT.0000000000000479>.
27. Frostell A, Hakim R, Thelin EP, Mattsson P, Svensson M. A review of the segmental diameter of the healthy human spinal cord. *Front Neurol.* 2016;7:238. <https://doi.org/10.3389/fneur.2016.00238>.
28. Gupta V. Positron emission tomography in spinal cord disease. *Mayo Clin Proc.* 2013;88:1188–90. <https://doi.org/10.1016/j.mayocp.2013.09.004>.
29. Tsutsui Y, Awamoto S, Himuro K, Umezu Y, Baba S, Sasaki M. Edge artifacts in point spread function-based PET reconstruction in relation to object size and reconstruction parameters. *Asia Ocean J Nucl Med Biol.* 2017;5:134–43. <https://doi.org/10.22038/aojnmb.2017.8802>.
30. Bartanusz V, Jezova D, Alajajian B, Digicaylioglu M. The blood-spinal cord barrier: morphology and clinical implications. *Ann Neurol.* 2011;70:194–206. <https://doi.org/10.1002/ana.22421>.
31. Li S, Cai Z, Wu X, Holden D, Pracitto R, Kapinos M, et al. Synthesis and in vivo evaluation of a novel PET radiotracer for imaging of synaptic vesicle glycoprotein 2A (SV2A) in nonhuman primates. *ACS Chem Neurosci.* 2019;10:1544–54. <https://doi.org/10.1021/acschemneuro.8b00526>.
32. Wang X, Duffy P, McGee AW, Hasan O, Gould G, Tu N, et al. Recovery from chronic spinal cord contusion after Nogo receptor intervention. *Ann Neurol.* 2011;70:805–21. <https://doi.org/10.1002/ana.22527>.
33. Imamoto N, Momosaki S, Fujita M, Omachi S, Yamato H, Kimura M, et al. [11C]PK11195 PET imaging of spinal glial activation after nerve injury in rats. *Neuroimage.* 2013;79:121–8. <https://doi.org/10.1016/j.neuroimage.2013.04.039>.
34. Tremoleda JL, Thau-Zuchman O, Davies M, Foster J, Khan I, Vadivelu KC, et al. In vivo PET imaging of the neuroinflammatory response in rat spinal cord injury using the TSPO tracer [(18)F]GE-180 and effect of docosahexaenoic acid. *Eur J Nucl Med Mol Imaging.* 2016;43:1710–22. <https://doi.org/10.1007/s00259-016-3391-8>.

Publisher's Note

Springer Nature remains neutral with regard to jurisdictional claims in published maps and institutional affiliations.

Submit your manuscript to a SpringerOpen[®] journal and benefit from:

- Convenient online submission
- Rigorous peer review
- Open access: articles freely available online
- High visibility within the field
- Retaining the copyright to your article

Submit your next manuscript at ► [springeropen.com](https://www.springeropen.com)
